Supplementary Material

Dual-modulation difference stimulated emission depletion microscopy to suppress the background signal

Wensheng Wang[1,†], Chuankang Li[1,†], Zhengyi Zhan[1], Zhimin Zhang[1], Yubing Han[1], Cuifang Kuang[1,2,3,4,*], and Xu Liu[1,2]

[1]*State Key Laboratory of Modern Optical Instrumentation, College of Optical Science and Engineering, Zhejiang University, Hangzhou, Zhejiang 310027, China*
[2]*Collaborative Innovation Center of Extreme Optics, Shanxi University, Taiyuan, Shanxi 030006, China*
[3]*Research Center for Intelligent Chips and Devices, Zhejiang Lab, Hangzhou, Zhejiang 311121, China*
[4]*Ningbo Research Institute, Zhejiang University, Ningbo, Zhejiang 315100, China*
[*]*Correspondence: Cuifang Kuang (cfkuang@zju.edu.cn)*
[†]*These authors contributed equally*

Outline

Supplementary Note1: The sketch review of the background removal techniques

Supplementary Note2: The theory deduction of dmdSTED

Supplementary Note3: Frequency spectrum distribution analysis

Supplementary Note4: Imaging simulation results of dmdSTED

Supplementary Note5: Supplementary experimental results of dmdSTED

Supplementary Note1

In this section, we introduce and compare those methods throughout the past decade that are effective in background removal of STED imaging. **Table S1** shows the comparison of those approaches along the time axis. **Table S2** presents the comparison of four types according to different domains.

Table S1 The comparison of background suppression techniques in STED

Year	Journal	Author	Technique Abbreviation	Method	Domain	Background Suppression Category *	Speed	Versatility	Simplicity	Reference
2012	Opt. Express	G. Vicidomini et al.	P-STED	Time-gating	Time domain	1	★★★	★★	★★	[10]
2013	Opt. Express	E. Ronzitti et al.	modSTED	Lock-in detection	Time domain	1	★	★★★	★★	[18]
2014	J. Biophotonics	I. Hernandez	gCW-STED	Time-gating	Time domain	1	★★★	★★	★★	[11]
2015	Nat. Commun.	J. Hanne et al.	QD STED	Double scanning	Space domain	1	★	★★★	★★★	[14]
2015	Nat. Commun.	L. Lanzano et al.		SPLIT	phasor domain	1+2	★★	★★	★★	[21]
2016	J. Phys. D: Appl. Phys.	M. Bordenave et al.		Time-gating	Time domain	1	★★★	★★★	★★	[12]
2017	Rev. Sci. Instrum.	M. Castello et al.	FPGA gSTED	Time-gating	Time domain	1	★★★	★★★	★	[13]
2017	Nat. Photonics	P. Gao et al.	STEDD	Double scanning	Space domain	1+2	★	★	★	[15]
2017	Opt. Lett.	P. Gao et al.	STEDD	Double scanning	Space domain	1+2	★	★	★	[16]
2018	Nat. Commun.	M. Sarmento et al.	M-STED	SPLIT	Phasor domain	1+2	★★	★★	★★	[22]
2018	Nanoscale	L. Wang et al.		SPLIT	Phasor domain	1+2	★★	★★	★★	[23]
2019	ACS Photonics	J. Lee et al.	psSTED	Double scanning	Space domain	1+2	★	★★	★★★	[17]
2019	Nanoscale	G. Tortarolo et al.	pSTED-SPLIT	SPLIT	Phasor domain	1+2	★★	★★	★★	[24]
2020	Laser Phton. Rev.	Y. Chen et al.		SPLIT	Phasor domain	1+2	★★	★★	★★	[25]
2020	J. Phys. D: Appl. Phys.	S. Pelicci et al.		SPLIT	Phasor domain	1+2	★★	★★	★★	[26]
2022		W. Wang et al.	dmdSTED	Lock-in detection	Frequency domain	1+2	★★	★★★	★★	

*Background Suppression Category: 1. re-excitation by STED; 2. incomplete depletion fluorescence

Table S2 The comparison of background suppression techniques based on four domains

Method	Subtractive Equation	Dyes	Bio-structures	Resolution	2D/3D	Advantage**	Disadvantage**
Time-domain method	$I=I_{open}-I_{close}$ $I=I_{T1}-\alpha I_{T2}$	Alexa Fluor 488 Oregon Green 488 ATTO 594 ATTO 647N	PtK2 cell microtubules, HeLa cell microtubules, HEK cell microtubules	$\lambda/12$	2D	i) Easy-to-implement setup ii) High resolution	i) Risk of signal loss; ii) Pulsed excitation is required iii) Required TCSPC hardware
Space-domain method	$I=I_{STED}-\alpha I_{solid}$ $I=I_{STED}-I_{hollow}$ $I=I_{STED1}-\alpha I_{STED2}$	ATTO 594 ATTO 647N Qdot705	U373 human astrocytes microtubules Rat embryonic fibroblasts vimentin fibres COS-7 cell microtubular cytoskeleton	$\lambda/8$	2D,3D	Without need for strong laser power	i) Doubled acquisition time; ii) Risk of image distortion
Phasor-domain method	$I=I_{long}-\alpha I_{short}$ $N_1=N-N_2-N_{BKGD}$	Alexa Fluor 488 Human Nup153 ATTO 647N	Hela cell microtubules Hela cell mitochondria	$\lambda/5$	2D	i) No need of a-priori spatial information; ii) Selective removal of backgrounds	i) Limited imaging resolution; ii) Required TCSPC hardware
Frequency-domain method	$I=I_{f1}-\alpha I_{f1\pm f2}$	ATTO 550 Star Green	Hela cell microtubules Hela cell vimentin	$\lambda/8$	2D	i) No need of post-processing ii) Effective removal of two backgrounds iii) Relatively high resolution	Required modulation hardware

**Only list the crucial advantages and disadvantages

Supplementary Note2

The basic principle of our method is shown in **Fig. 1**. For traditional STED (**Fig. 1a** and **Fig. 1b**), the excitation and depletion lasers are continuous or pulsed with a certain repetition frequency, so the final fluorescent signal keeps unfluctuating. For our method (**Fig. 1c**), we apply different modulation frequencies f_{m1} and f_{m2} to the excitation and depletion beams respectively. When two lasers of different frequencies are focused to the sample, signals with multiple frequencies will be obtained. This can be explained through investigating the differential rate equation of the fluorescence process. Here, we consider a five-level photophysical model of fluorescence as shown in **Fig. S1a**. S_0, S_1 and T_1 represent the ground singlet state, first-excited singlet state and lowest-excited triplet state, respectively. S_n and T_n are the higher excited singlet and triplet states, respectively. The fluorescence signal is proportional to the population of the fluorescent molecules in S_1.

When the photobleaching phenomenon is not considered, the temporal populations of each level can be obtained by solving the rate equations[32–33]:

$$
\begin{cases}
S_0 = S_1 k_f + k_T T_1 - S_0 k_{exc} \\
S_1 = S_0 k_{exc} + k_{n1} S_n - S_1 (k_0 + k_{1n}) \\
T_1 = S_1 k_{isc} + k_{Tn1} T_n - T_1 (k_T + k_{T1n}) \\
S_n = S_1 k_{1n} - k_{n1} S_n \\
T_n = T_1 k_{T1n} - k_{Tn1} T_n
\end{cases}
\tag{S1}
$$

where k_{mn} represents the quantitative rate constant from the state m to n. k_f, k_T, and k_{isc} represent the de-excitation rate constants of S_1 through fluorescence, de-excitation rates of T_1, and intersystem crossing to T_1, respectively. Here the fluorescence lifetime can be obtained as:

$$
\tau_0 = \frac{1}{k_0} = \frac{1}{k_f + k_{isc}}
\tag{S2}
$$

Considering that S_n and T_n are usually much smaller than other states, the equations can be further simplified to three-level energy equations, and the populations of each electronic state can be approximately determined by the steady-state population probabilities. Hence, the explicit function of equivalent probability of S_1 can be expressed as:

$$
S_1 = \frac{k_{exc}}{k_{exc}(1 + k_{isc}/k_T) + k_0}
\tag{S3}
$$

Then considering the depletion beam and stimulated emission effect into the fluorescence process, the equivalent probability of S_1 can be rewritten as:

$$
S_1 = \frac{k_{exc}}{k_{exc}(1 + k_{isc}/k_T) + k_0 + k_{STED}}
\tag{S4}
$$

where k_{STED} represents the rate constant of stimulated emission process. In order to be more specific, we would take Rhodamine 6G as example to simulate this process, then the value of k_{isc}, k_T and k_0 are 1.1×10^6 s^{-1}, 4.9×10^5 s^{-1}, and 2.56×10^8 s^{-1}, respectively.

We apply the sinusoidal modulation with different frequencies f_{m1} and f_{m2} to the excitation beam and the depletion beam, respectively. Here we define the modulation contrast $CM = (I_{max} - I_{min})/(I_{max} + I_{min})$, where I_{max} or I_{min} is the maximum intensity or minimum intensity of the excitation or depletion beam. Thus, the applied frequency functions of the excitation beam and the depletion beam, $f_{m1}(t)$ and $f_{m2}(t)$, can be expressed as follows:

$$
f_{m1}(t) = 1 + CM_1 \cos(2\pi f_{m1}t)
\tag{S5}
$$

$$
f_{m2}(t) = 1 + CM_2 \cos(2\pi f_{m2}t)
\tag{S6}
$$

where CM_1 and CM_2 are the modulation contrast of the excitation and depletion beams, respectively. To this end, the modified equivalent probability of S_1 with light intensity modulation can be written as:

$$S_1' = \frac{k_{exc} f_{m1}(t)}{k_{exc} f_{m1}(t)(1 + k_{isc}/k_T) + k_0 + k_{STED} f_{m2}(t)} \quad \text{(S7)}$$

Generally, the anti-Stokes excitation or the re-excitation caused by the depletion beam tends to co-exist with the normal fluorescence excitation. Its rate constant is k_{STED}^{RE} and the equivalent probability is shown:

$$S_1^* = \frac{k_{exc} f_{m1}(t) + k_{STED}^{RE} f_{m2}(t)}{(k_{exc} f_{m1}(t) + k_{STED}^{RE} f_{m2}(t))(1 + k_{isc}/k_T) + k_0 + k_{STED} f_{m2}(t)} \quad \text{(S8)}$$

Note that the population in the excited state caused by anti-Stokes excitation (AStEx) is easily derived:

$$S_1^{RE} = \frac{k_{STED}^{RE} f_{m2}(t)}{(k_{exc} f_{m1}(t) + k_{STED}^{RE} f_{m2}(t))(1 + k_{isc}/k_T) + k_0 + k_{STED} f_{m2}(t)} \quad \text{(S9)}$$

The emission intensity is proportional to S_1^*. The fluorescence intensity I_{fluor} can be written using a scaling factor C between the population in the excited state and the emitted photon number:

$$I_{fluor} = C \cdot S_1^* \quad \text{(S10)}$$

Applied with Fourier transform, we transfer the signal intensity information into the spatial frequency intensity $\xi(f)$ which is dependent with the discrete frequency ranging from negative infinity to positive infinity:

$$\xi(f) = FFT\{I_{fluor}\} \quad \text{(S11)}$$

We nominate the fundamental frequency f_1 (equal to modulation frequency f_{m1} of the excitation beam) and the harmonic frequency f_2 (equal to the modulation frequency f_{m2} of the depletion beam). In like manner, the sum frequency $(f_1 + f_2)$, the difference frequency $(f_1 - f_2)$, the double frequency $(2f_1)$, and the triple frequency $(3f_1)$ are nominated. From above formula, the frequency spectrum distribution is acquired (**Fig. S1b**). Notably, the frequency components in negative coordinate is virtually non-existent. The segment length in each frequency represents the reciprocal signal strength. The applied modulation frequencies of the excitation beam and the depletion beam are 10 kHz and 15 kHz. The simulation result shows the following signal strengths: fundamental frequency intensity $\xi(f_1)$, harmonic frequency intensity $\xi(f_2)$, sum frequency intensity $\xi(f_1 + f_2)$, difference frequency intensity $\xi(f_1 - f_2)$, double frequency intensity $\xi(2f_1)$, triple frequency intensity $\xi(3f_1)$, and the remnant signals.
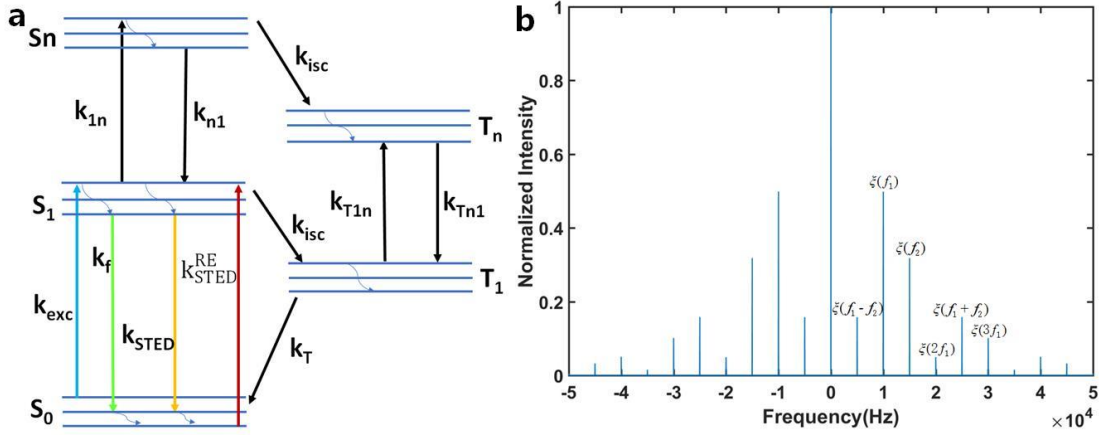
Fig. S1 a Diagrams of five energy levels and photophysical model of fluorescent molecules. **b** The frequency spectrum distribution by Fourier transform of the acquired equivalent probability at the molecular energy state S_1.

When $f = 0$, its frequency intensity is considered to be ignored because it relates to the inherent frequency of the optics system which is of direct current (DC) signal. The total frequency intensity is thus obtained as follows:

$$\zeta_{total} = \left[\sum_{-\infty}^{+\infty} \xi(f) - \xi(0) \right] \Big/ 2 \tag{S12}$$

Thus, we define signal intensity ratio (SIR) as the ratio between each intensity at specific frequency component between the total frequency intensity:

$$SIR = \xi(f) / \zeta_{total} \tag{S13}$$

When applying an $f_{m1} = 10$ kHz sinusoidal modulation to the excitation beam ($I_{exc} = 3$ kW/cm^2, $CM_1 = 1$) and an $f_{m2} = 15$ kHz sinusoidal modulation to the depletion beam ($I_{dep} = 100$ MW/cm^2, $CM_2 = 0.67$), the signal intensity ratios (SIR) of the as-nominated signals are all larger than 3% (seen from **Fig. S2**). The total remaining signal intensity is less 3% which is thereby considered to be negligible to our research. It can be seen that fluorescence signals (including effective signal, anti-Stokes background, non-depleted fluorescence) appear at several different frequencies. **Fig. 1d** and **Fig. 1e** show the schematic illustration of effective signal, anti-Stokes background and non-depleted fluorescence between space domain and frequency domain.
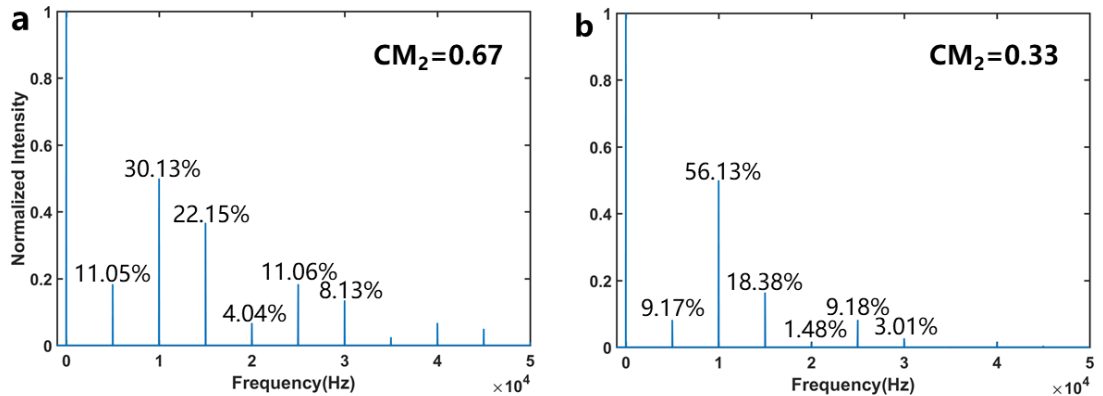
Fig. S2 a Frequency spectrum distribution when $CM_2 = 0.67$. **b** Frequency spectrum distribution when $CM_2 = 0.33$.

In the center of the PSF where only the modulated excitation beam acts, $\xi(f_1)$ corresponds to the effective signal and the non-depleted fluorescence. In the peripheral of the

PSF where the modulated excitation and depletion beams act together, $\xi(f_1 - f_2)$ or $\xi(f_1 + f_2)$ corresponds only to the non-depleted fluorescence. Note that $\xi(f_2)$ corresponds to anti-Stokes background and non-depleted fluorescence. For anti-Stokes background, while a lock-in detection is utilized to demodulate the frequencies f_1, f_1+f_2, f_1-f_2, this uncorrelated background is filtered by hardware. Ideally, $\xi(2f_1)$ and $\xi(3f_1)$ consist of the same fluorescence as $\xi(f_1)$. For simplicity in theory, we neglect those components. For further reading, one can refer to **Supplementary Note3**.

Thus, our dmdSTED can be easily acquired by the subtraction between the fundamental frequency intensity and the sum or difference frequency intensity using a subtraction coefficient α. The optimal subtraction coefficient is around 1.5 (see **Fig. S11** in **Supplementary Note4**). Note that the difference process is fulfilled by lock-in detection and software so that the temporal resolution is not compromised. For each pixel, dmdSTED result is derived as:

$$\xi_{dmdSTED}(f) = \xi(f_1) - \alpha \cdot \xi(f_1 \pm f_2) \tag{S14}$$

The frequency intensity scales with the space-domain signal intensity using a scaling factor. Hence, the two-dimensional frequency-dependent intensity point spread function (PSF) is calculated as:

$$PSF_{dmdSTED}(x, y, f) = D \cdot \xi_{dmdSTED}(f) \cdot PSF_{conf} \otimes P(x, y) \tag{S15}$$

where PSF_{conf} is the PSF for confocal mode, $P(x, y)$ is the pupil function of the confocal pinhole, and D denotes to the scaling factor between the frequency signal intensity and the space-domain signal intensity. Thus, using the molecule sample $S(x, y)$, the final imaging is expressed as:

$$F_{dmdSTED}(x, y, f) = PSF_{dmdSTED}(x, y, f) \otimes S(x, y) \tag{S16}$$

Supplementary Note3

Seen from **Fig. S2**, change of parameters, like modulation contrast (CM_1 and CM_2), will alter the frequency spectrum distribution. Other factors, like excitation beam intensity (I_{exc}), depletion beam intensity (I_{dep}), and the applied modulation frequency (f_{m1} or f_{m2}), are equally important to the further understanding of dmdSTED. Those parameters are explicitly investigated and the numerical results, as well as some experimental results, are shown in **Figs. S3–S7**.

In **Fig. S3**, the fundamental frequency ratio negatively correlates with CM_2. The ratios of other frequency components increase with the improvement of CM_2. Note that the curve of the harmonic frequency presents a maximum when CM_2 is around 0.6–0.8. From **Fig. S7a**, it is seen that higher CM_2 yields higher harmonic frequency signal intensity, especially when $CM_2 = 0.8$. From **Fig. S7b**, it is concluded that the excitation beam intensity almost has no effect on the fundamental frequency signal intensity. Additionally, higher modulation frequency on I_{exc} yields larger fundamental frequency signal intensity, especially when $f_{m1} = 400$ kHz. Also, it is concluded that the excitation beam intensity almost has no effect on the fundamental frequency signal intensity except for the cases of f_2 larger than 100 kHz (**Fig. S7c**). From **Fig. S7d**, it is seen that higher CM_2 yields higher harmonic frequency signal intensity, especially when $CM_2 = 0.8$.
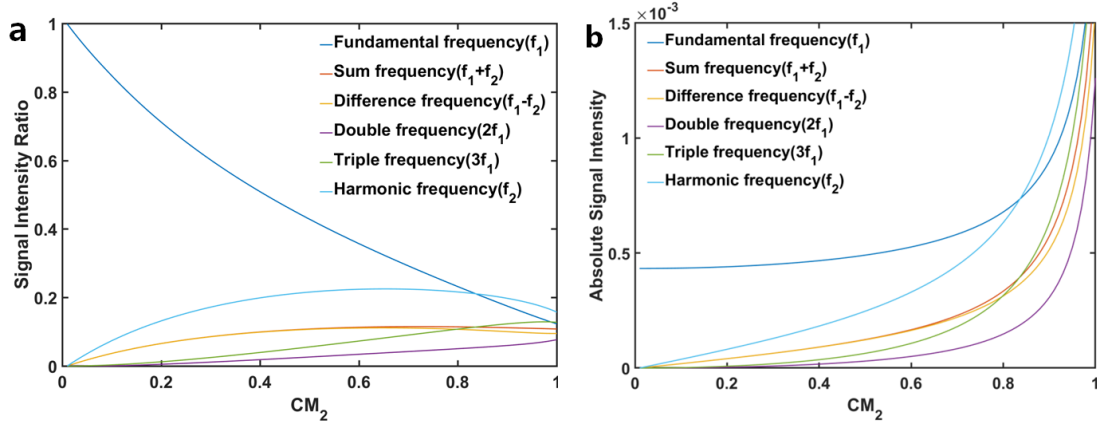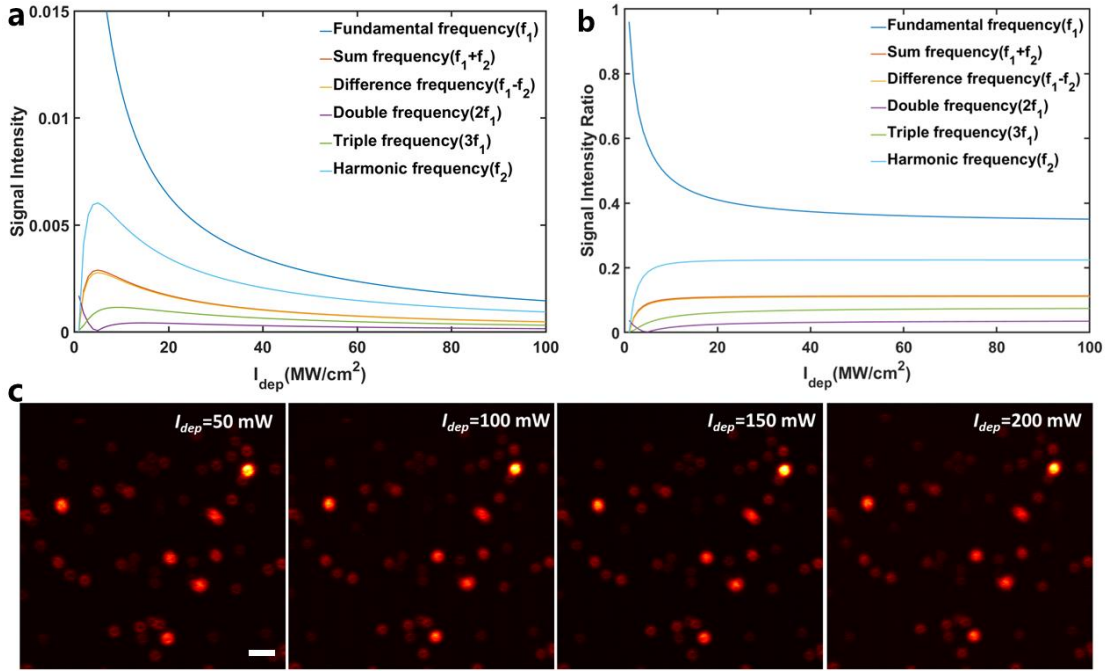
Fig. S3 a The influence of modulation contrast (CM_2) of the depletion beam against the signal intensity ratio of different frequency components. **b** The influence of CM_2 against the absolute signal intensity of different frequency components. With the increment of CM_2, the inhibition effect of the depletion illumination has been diminished so that all signal components show an upward trend. The excitation beam intensity I_{exc} = 10 kW/cm^2; the depletion beam intensity I_{dep} = 100 MW/cm^2; modulation contrast of the excitation beam CM_1 = 1; modulation frequency for the excitation beam f_{m1} = 10 kHz; modulation frequency for the depletion beam f_{m2} = 15 kHz.
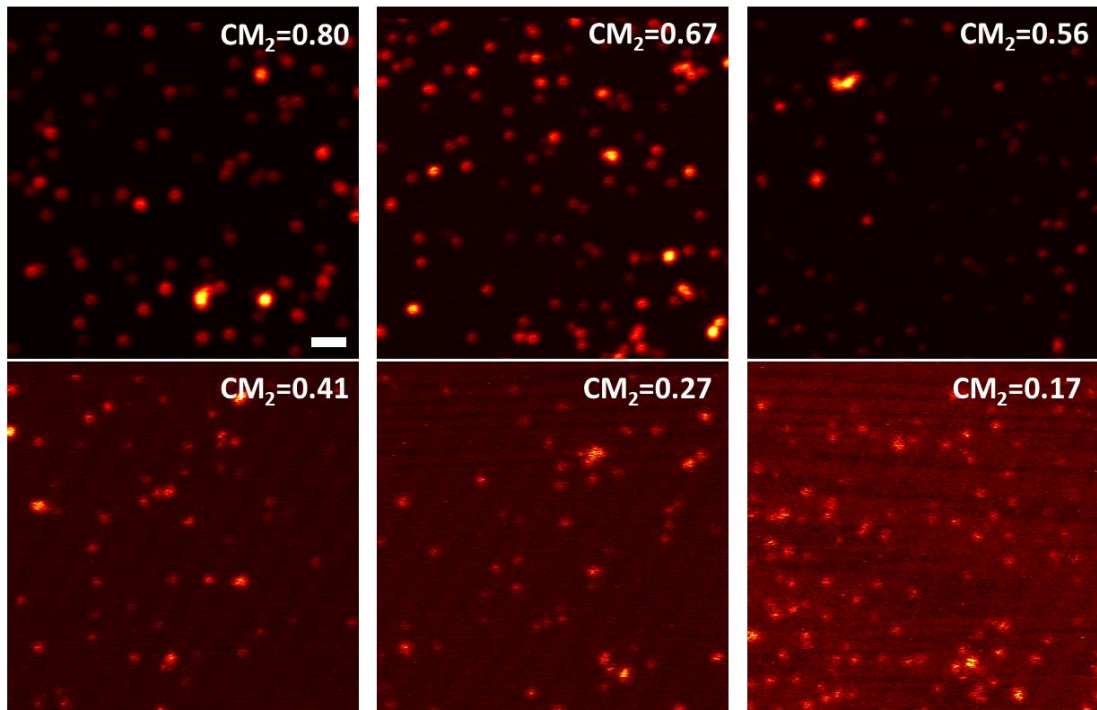
Fig. S4 The experimental results of imaging of $\xi(f_1 - f_2)$ when different CM_2 values are employed. The images testify the simulations in **Fig. S3a**. Scale bar: 500 nm.
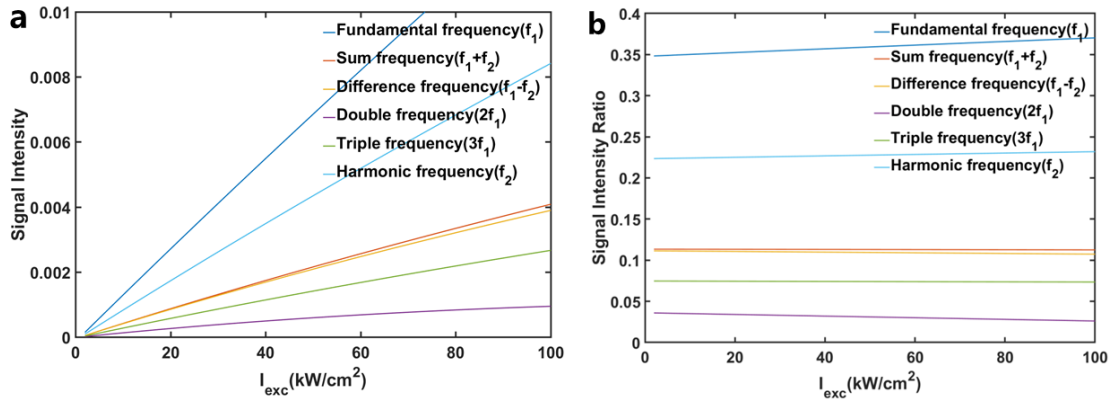
Fig. S5 a The influence of excitation intensity I_{exc} against the signal intensities $\xi(f)$ of different frequency components. Generally, those signal intensities linearly correlate with the excitation beam intensity. **b** The influence of I_{exc} against the signal intensity ratio of different frequency components. The simulation result shows that each signal component ratio maintains an unchanging value. We can also conclude that the excitation intensity could have little effect on our dmdSTED method.

Fig. S6 a The influence of depletion intensity I_{dep} against the signal intensities $\xi(f)$ of different frequency components. It is seen that all those signal components are inhibited due to the increase of the depletion power. Additionally, the higher of the depletion beam intensity, the more inhibition of the f_1 component. **b** The influence of I_{dep} against the signal intensity ratio of different frequency components. The total ratio of those frequency components approaches 1. **c** The experimental results of imaging of $\xi(f_1 - f_2)$ when different I_{dep} values are employed. The images testify the simulations in **b**. Scale bar: 500 nm.
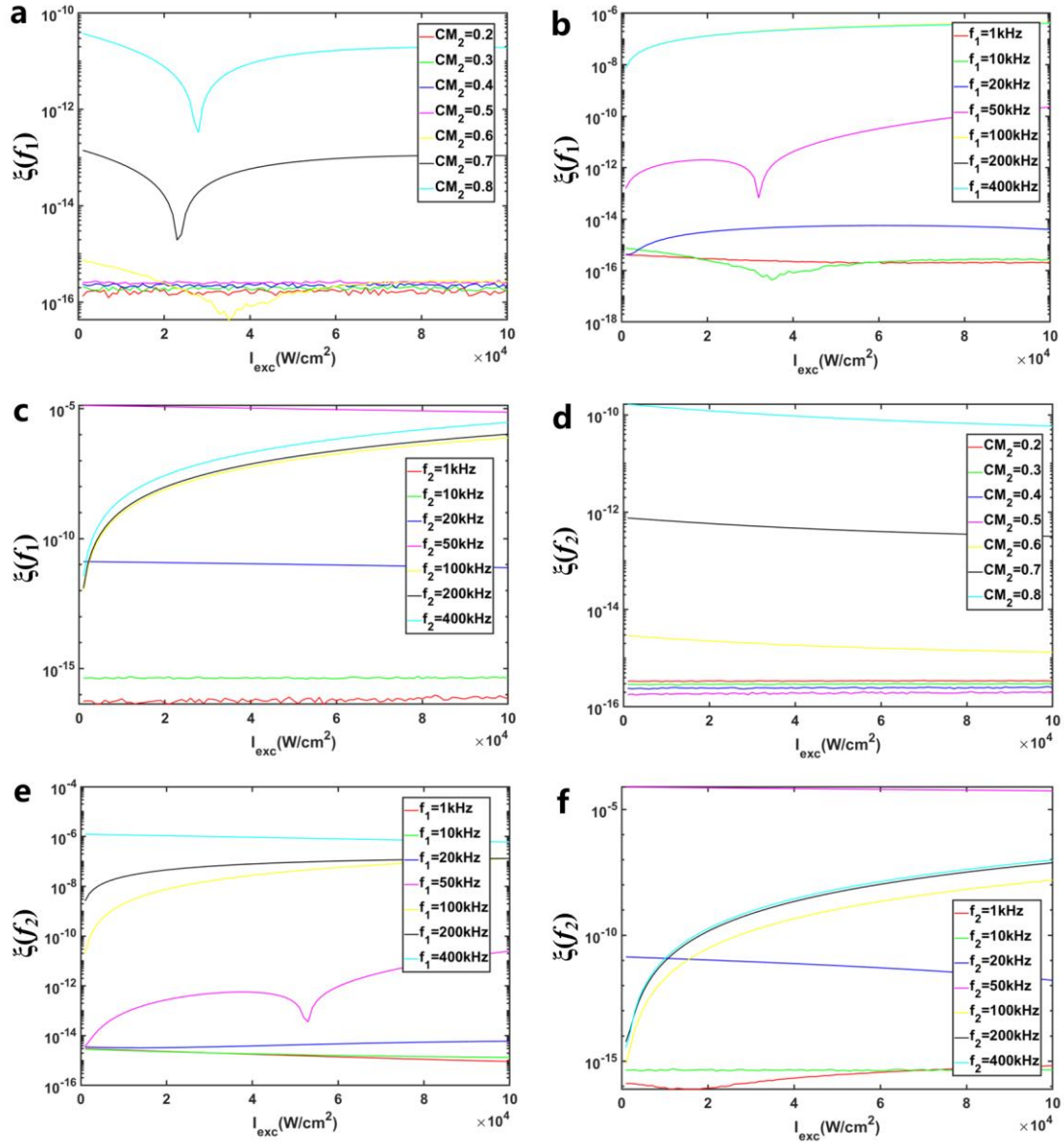
Fig. S7 a The influence of excitation intensity I_{exc} against the signal intensity of fundamental frequency $\xi(f_1)$ component in cases of different modulation contrast (CM_2) of the depletion beam. The modulation frequency for the excitation beam $f_1 = 10$ kHz; modulation frequency for the depletion beam $f_2 = 15$ kHz. **b** The influence of I_{exc} against $\xi(f_1)$ in cases of different modulation frequencies f_{m1} when $CM_2 = 0.6$ and $f_{m2} = 15$ kHz. **c** The influence of I_{exc} against $\xi(f_1)$ in cases of different modulation frequencies f_{m2} when $CM_2 = 0.6$ and $f_{m1} = 10$ kHz. **d** The influence of I_{exc} against the signal intensity of harmonic frequency $\xi(f_2)$ component in cases of different CM_2 values. Other parameters: $f_{m1} = 10$ kHz; $f_{m2} = 15$ kHz. **e** The influence of I_{exc} against $\xi(f_2)$ in cases of different f_{m1} when $CM_2 = 0.6$ and $f_{m2} = 15$ kHz. **f** The influence of I_{exc} against $\xi(f_2)$ in cases of different f_{m2} when $CM_2 = 0.6$ and $f_{m1} = 10$ kHz.
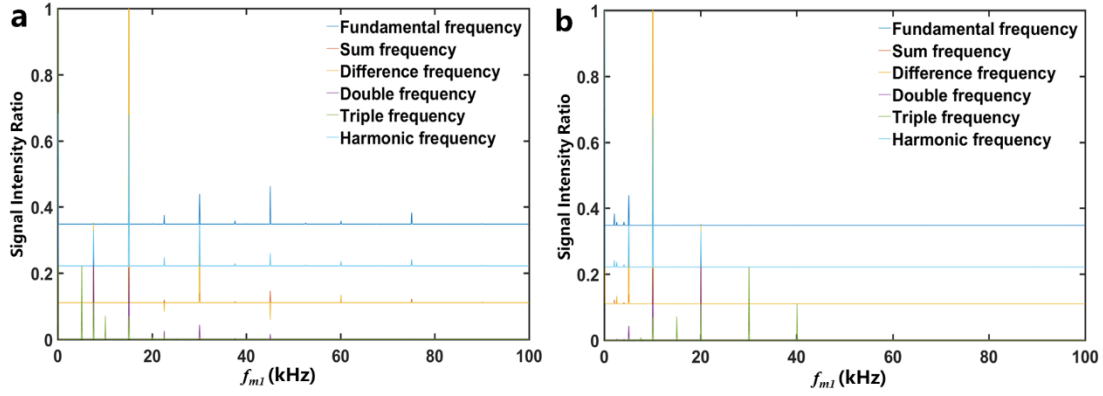
Fig. S8 a The influence of f_{m1} (from 1 to 100 kHz) against different frequency components when $f_{m2} = 15$ kHz. **b** The influence of f_{m2} (from 1 to 100 kHz) against different frequency components when $f_{m1} = 10$ kHz.. Other parameters: $I_{exc} = 10$ kW/cm^2; $I_{dep} = 100$ MW/cm^2.

Supplementary Note4

In this section, we discuss the dmdSTED imaging results. **Figs. S9-S10** show PSF comparison between imagings acquired by different frequency components.

We also investigate the influence of subtracting coefficient (**Fig. S11**). In order to perform best, the negative value should be around 0, and the achieved resolution is 30 nm. Thus, the optimal subtracting coefficient is around 1.5.

The applied parameters are as follows: $I_{exc} = 10$ kW/cm^2; $I_{dep} = 100$ MW/cm^2; $f_{m1} = 10$ kHz; $f_{m2} = 15$ kHz; $CM_2 = 0.9$. The same parameters are for **Figs. S12–S13** in which densely -distributed nanoparticle and microtube numerical works are conducted. In **Fig. S14**, modulation transfer function (MTF) simulation is carried out which clarifies the resolution ability of dmdSTED in frequency domain. The relationship between MTF and the spatial frequency is by normalization of the value of $2\pi NA/\lambda$, where NA denotes to numerical aperture of the optics and λ corresponds to the illumination wavelength.
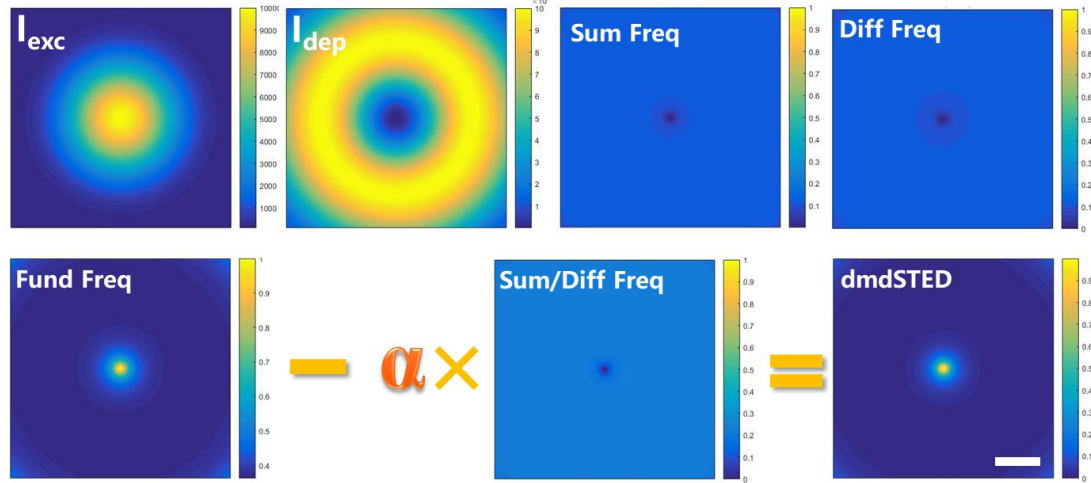

Fig. S9 Point spread function (PSF) of the excitation beam, the depletion beam, and different frequency components. Sum Freq: sum frequency component; Diff Freq: difference frequency component; Fund Freq: fundamental frequency component; Scale bar for all images: 100 nm.
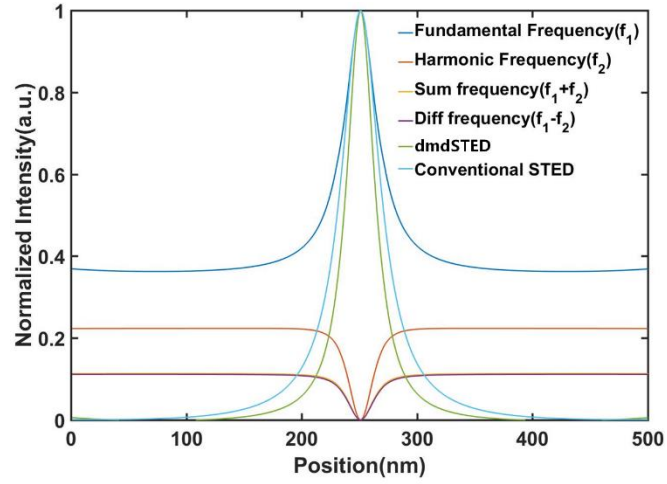
Fig. S10 Line plot of the normalized intensities of the conventional STED, different frequency components, and dmdSTED. The values of sum frequency and difference frequency are almost equal.
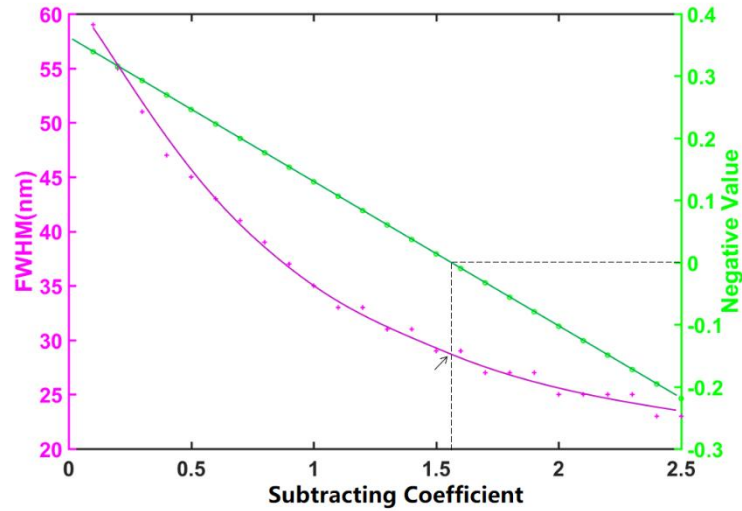

Fig. S11 The influence of the subtracting coefficient against FWHM and the negative value of resulting imaging via dmdSTED. $I_{exc} = 10$ kW/cm^2; $I_{dep} = 100$ MW/cm^2; $CM_1 = 1$, $CM_2 = 0.6$; $f_{m1} = 10$ kHz; $f_{m2} = 15$ kHz. From the simulative result, the optimal subtracting coefficient is 1.56 in order for the balance of FWHM and negative value. In the practical experiment, this optimal value is also testified to be feasible (refer to **Fig. 3**).
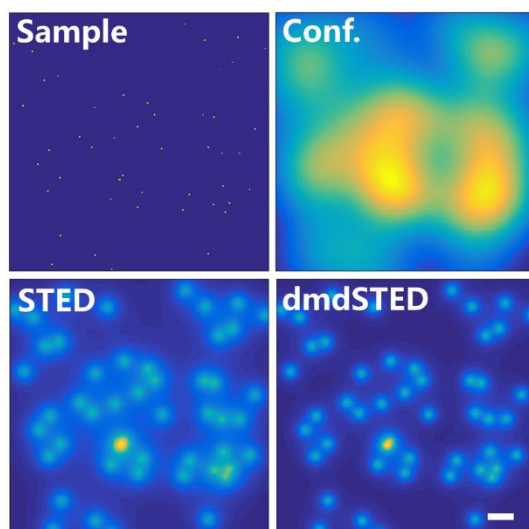
Fig. S12 Molecule imaging results with high nanoparticle density: sample, confocal, conventional STED, and dmdSTED. The molecule number: 60. In densely-distributed molecule ambient, the resolution of dmdSTED is improved compared with the conventional STED imaging. Scale bar for all images: 100 nm.
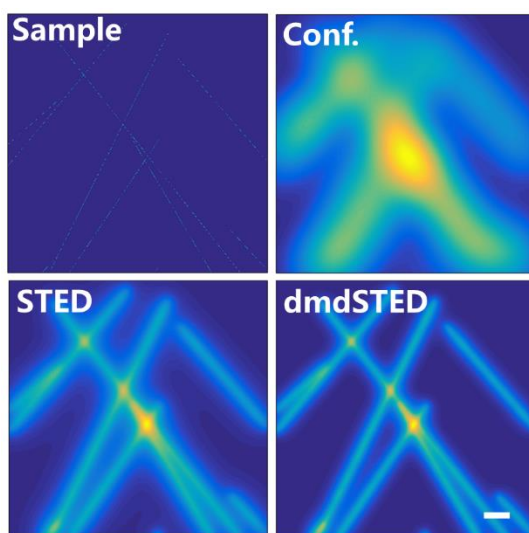
Fig. S13 Microtube imaging results: sample, confocal, conventional STED, and dmdSTED. This simulation work is of reference to real-world imaging of cell microtubes. Scale bar for all images: 100 nm.
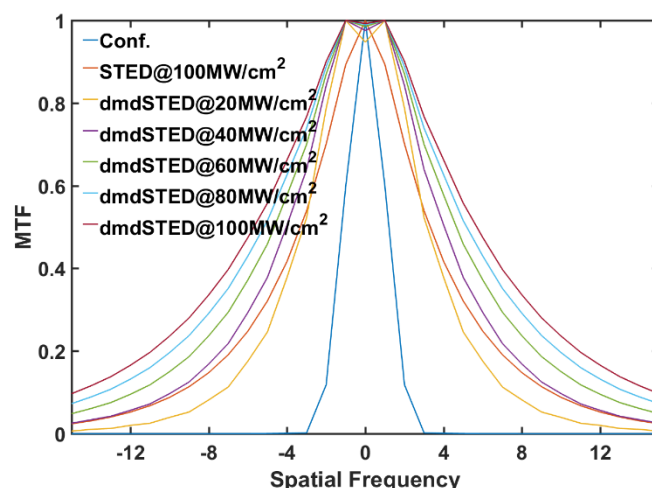
Fig. S14 Modulation transfer function (MTF) of different imaging techniques: confocal, conventional STED, dmdSTED with different depletion intensities ranging from 20 to 100 MW/cm^2. Other parameters: $f_{m1} = 10$ kHz; $f_{m2} = 15$ kHz; $CM_2 = 0.9$.
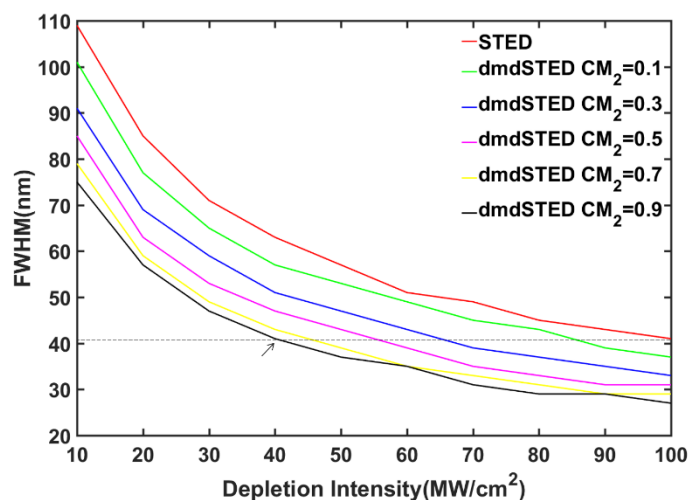
Fig. S15 The influence of the depletion intensity on the full width half maximum (FWHM) of the imaging results via different techniques: conventional STED and dmdSTED with different CM_2 values ranging from 0.1 to 0.9.

Supplementary Note5

Preparation of perovskite samples

Cs_2CO_3 (99.9%), $PbBr_2$ (99.9%), oleic acid (OA, technical grade 90%), and oleylamine (OAm, technical grade 70%) were purchased from Sigma-Aldrich (St. Louis, MO, USA). Octane was purchased from Maclin Biochemical Co. Ltd. (Shanghai, China). Hexane and acetone were purchased from Damao Chemical Works. All chemicals were used without further purification. One-pot synthetization of $CsPbBr_3$ NPs was performed by adding Cs_2CO_3 (0.1 mmol) and $PbBr_2$ (0.3 mmol) were added to a 100-*mL* round-bottom flask, followed by a mixture solution comprising 10 mL of octane, 0.5 mL of OA, and 0.5 mL of OAm. The flask was heated to 90 °C in a water bath. All reaction processes were conducted in the open air without any inert atmosphere. Colloidal nanocrystals were obtained after 30 min of the reaction. The obtained nanoparticle dispersions were left undisturbed for one day to precipitate large nanocrystals, and the supernatant was stored for later use.

Characterization of CsPbBr$_3$ NPs: The morphologies were observed using a Jeol JEM-1230 transmission electron microscope (JEOL, Tokyo, Japan) at the acceleration voltage of 100 kV. Photoluminescence spectra were measured using an OCEAN QS65000 spectrofluorometer (Ocean Optics, Dunedin, FL, USA) under excitation by 400-nm UV light.

Optics setup of dmdSTED

Figs. S16–S20 show the supplemented experimental results of dmdSTED. Exhibited in **Fig. S16**, the continuous-wave (CW) 488-nm excitation laser (Laser1, BDL-SMN-488, Thorlabs) was modulated using a solid-state acousto-optic modulator (AOM, AOMO 3080-125, Gooch & Housego), while another CW 592-nm depletion laser (Laser2, PFL-80-3000-775-B1R, MPB Communications Inc.) was modulated through an electro-optic modulator (EOM, 350-80BK-01, Conoptics Inc.). Both laser beams were tuned to circular polarization at the entrance pupil of the objective lens, and the depletion beam was exerted in the 0–2π phase by a vortex phase plate (VPP, vpp-1a, RPC photonics) to generate a doughnut-shaped light distribution at the focal surface of the objective lens. Both beams were then spatially combined and scanned through the sample using a scanning galvanometric mirror. The fluorescence signal was de-scanned by the galvanometric mirror and finally detected by a photomultiplier tube (PMT, H7422-50, Hamamatsu Photonics).

The technical parameters are as follows. Laser1, 488 nm laser, BDL-SMN-488, Thorlabs. Laser2, 592 nm laser, PFL-80-3000-775-B1R, MPB Communications Inc. AOM, acoustic-optic modulator, AOMO 3080-125, Gooch & Housego. RF, radio frequency driver, 1080AFP-AD-1.0, Gooch & Housego. FG, function generator. EOM, electro-optic modulator, 350-80BK, Conoptics. DR1, driver control, Model 275, Conoptics. LIA, lock-in amplifier, HF2LI, Zurich Instruments. VPP, vortex phase plate, vpp-1a, RPC Photonics. GM, galvanometer-based scanning mirrors. Piezo, Piezo sample stage, P-734, Physik Instrument. DR2, driver control, E-710, Physik Instrument. PBS, polarized beam splitter, Thorlabs. HWP, half wave plate, Thorlabs. QWP, quarter wave plate, Thorlabs. AQWP, achromatic quarter wave plate, Thorlabs. M, mirror, Thorlabs. T, telescope, Thorlabs. Pr, polarizer, Thorlabs. GT, Glan prism, Thorlabs. L, achromatic lens with VIS anti-reflection coating, Thorlabs. SL, scanning lens, SL50-CLS2, Thorlabs. TL, tube lens, TTL200MP, Thorlabs. OL, objective lens, Apo 100x/1.4 Oil, Leica. DM1, dichroic mirror, ZT488-532-592-647-750rpc, Chroma. DM2, dichroic mirror, ZT594dcrb, Chroma. F, filter, ZET488-532-592-647-750, Chroma. MMF, multi-mode fibre. PMT, photomultiplier tube, H7422PA-50, Hamamatsu Photonics. APD, avalanche diode, SPCM-AQRH-43-FC, Excelitas Technologies. TCSPC, time-correlated single photon counting system, PicoHarp 300, Picoquant. DAQ, data acquisition card, NI PCI-6366, National Instruments.

Experimental results of frequency response are shown in **Fig. S17**. This figure shows the fitting curve of the system frequency response, and the experimental interval is from 10 kHz to 250 kHz. The results provide the experimental ground of which we select the modulation frequency.
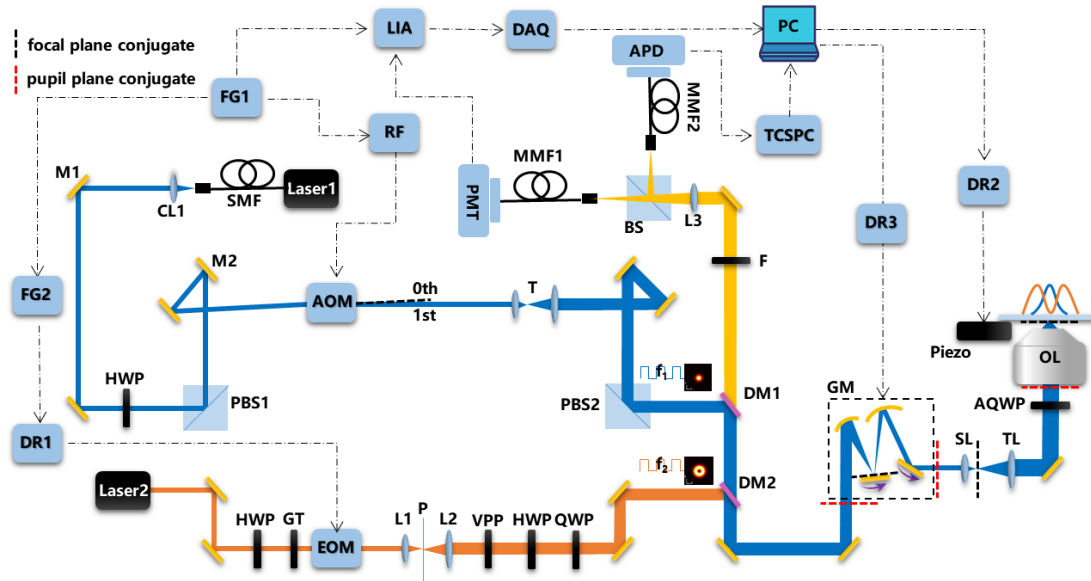
Fig. S16 Schematic setup of dmdSTED system.
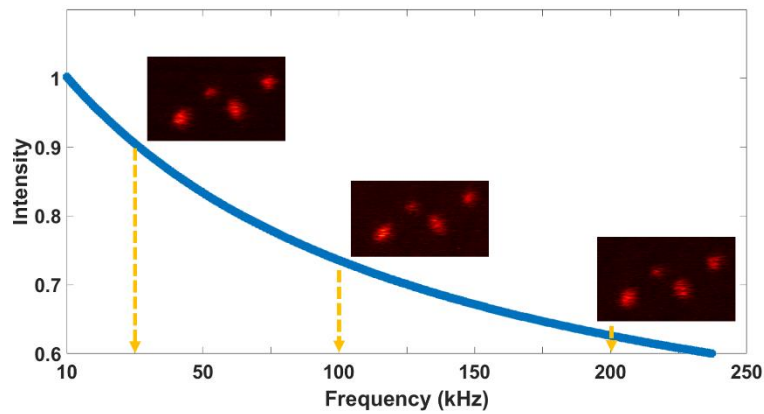
Fig. S17 The system frequency response. Due to the different detection effectivity at different frequencies, actual experiments must consider the frequency response at corresponding frequency interval. Indeed, it is recommended to adopt high frequency of f_m (above ~1 MHz) to avoid laser intensity noise which occurs primarily at low frequencies (from DC to kilohertz) in the form of the so-called $1/f_m$ noise. As f_m goes above the megahertz range, the laser intensity noise gradually approaches the floor of quantum shot noise, which is always present because of the Poissonian distribution of the photon counts at the detector. Therefore, the broad-band modulation/demodulation at f_m removes the low-frequency $1/f_m$ laser intensity noise and allows for shot-noise-limited detection sensitivity.
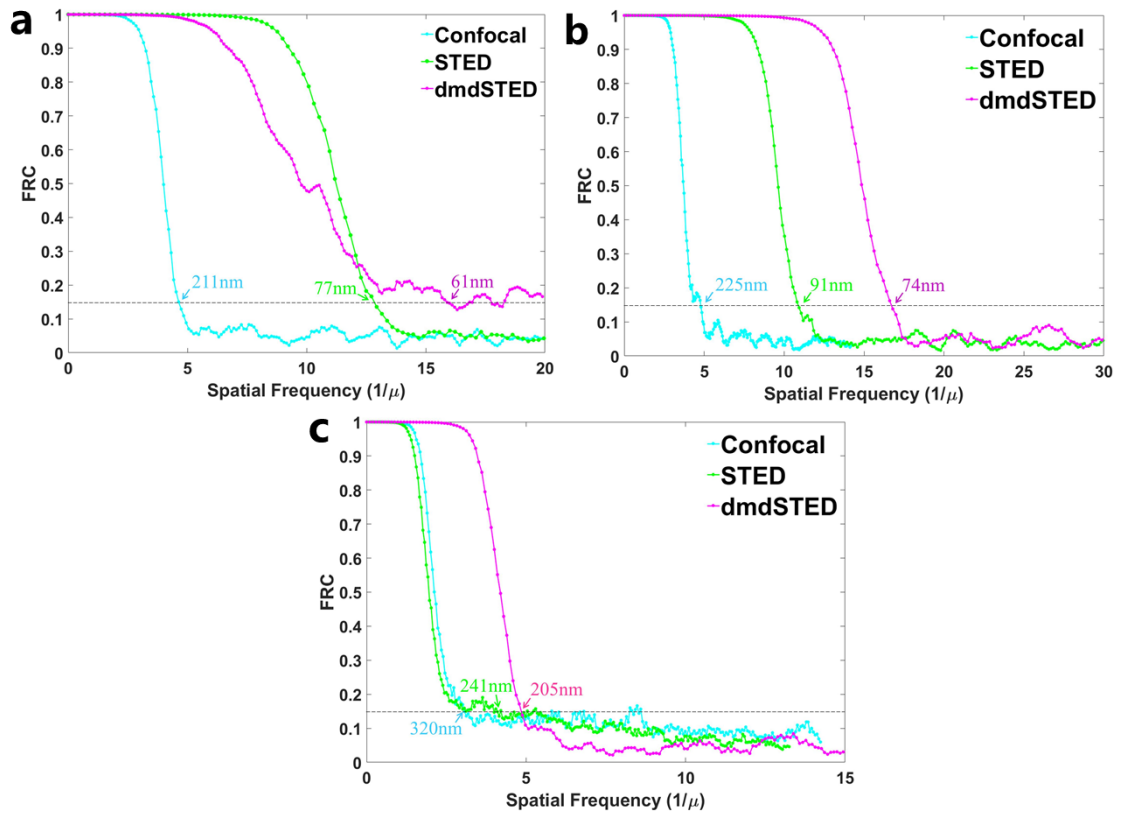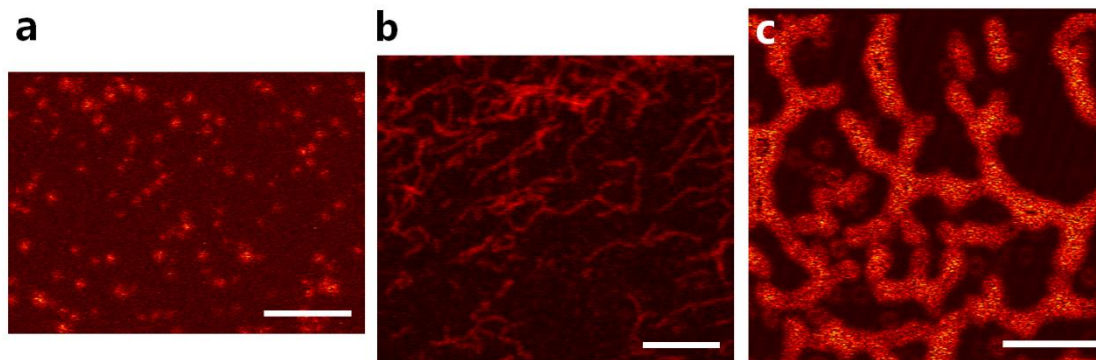
Fig. S18 Fourier ring correlation (FRC) analysis. **a** FRC profile of **Fig. 3**. **b** FRC profile of **Fig. 4**. **c** FRC profile of **Fig. 5**.
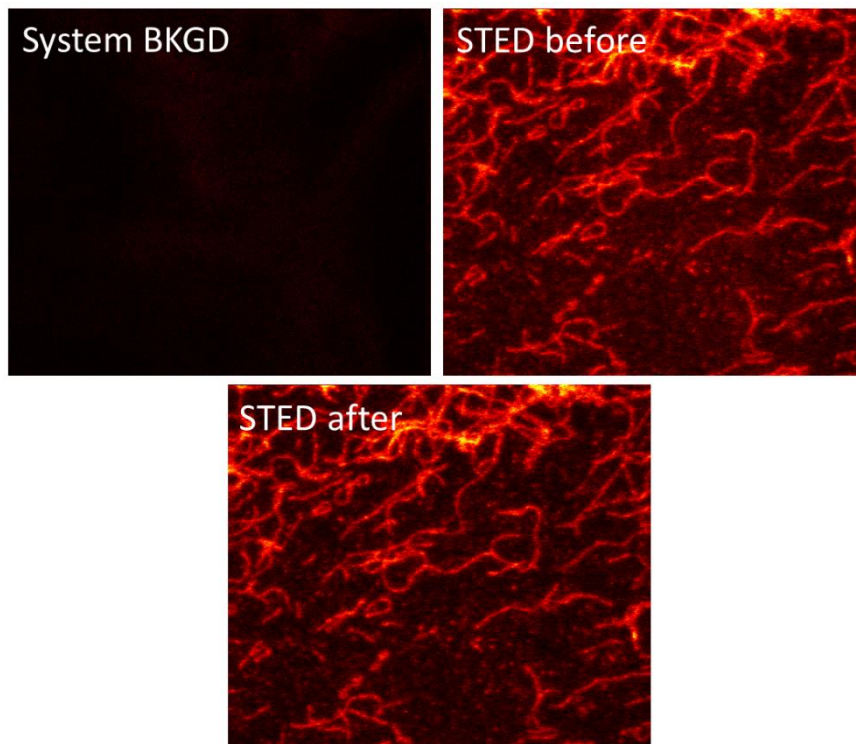
Fig. S19 The images show the system background, STED image before background removal, and STED image after background removal, respectively.

Fig. S20 The images presented the subtracted backgrounds for dmdSTED. **a** The background in **Fig. 3**. **b** The background in **Fig. 4**. **c** The background in **Fig. 5**. The backgrounds are acquired by demodulating at the frequency (f_1+f_2). The scale bars for all images: 2 μm.